Journal of
Manufacturing and Materials Processing

MDPI

Article

Improving the Quality of Reshaped EoL Components by Means of Accurate Metamodels and Evolutionary Algorithms

Antonio Piccininni [1,*], Angela Cusanno [1], Gianfranco Palumbo [1], Giuseppe Ingarao [2] and Livan Fratini [2]

[1] Department of Mechanics, Mathematics and Management, Politecnico di Bari, Via Orabona 4, 70125 Bari, Italy; angela.cusanno@poliba.it (A.C.); gianfranco.palumbo@poliba.it (G.P.)
[2] Department of Engineering, University of Palermo, Viale delle Scienze, 90128 Palermo, Italy; giuseppe.ingarao@unipa.it (G.I.); livan.fratini@unipa.it (L.F.)
* Correspondence: antonio.piccininni@poliba.it

Abstract: The reshaping of End-of-Life (EoL) components by means of the sheet metal forming process has been considered largely attractive, even from the social and economic point of view. At the same time, EoL parts can often be characterized by non-uniform thicknesses or alternation of work-hardened/undeformed zones as the result of the manufacturing process. Such heterogeneity can hinder a proper reshaping of the EoL part, and residual marks on the reformed blanks can still be present at the end of the reshaping step. In a previous analysis, the authors evaluated the effectiveness of reshaping a blank with a deep-drawn feature by means of the Sheet Hydroforming (SHF) process: it was demonstrated that residual marks were still present if the deep-drawn feature was located in a region not enough strained during the reshaping step. Starting from this condition and adopting a numerical approach, additional investigations were carried out, changing the profile of the load applied by the blank holder and the maximum oil pressure. Numerical results were collected in terms of overall strain severity and residual height of the residual marks from the deep-drawn feature at the end of the reshaping step. Data were then fitted by accurate Response Surfaces trained by means of interpolant Radial Basis Functions and anisotropic Kriging algorithms, subsequently used to carry out a virtual optimization managed by multi-objective evolutionary algorithms (MOGA-II and NSGA-II). Optimization results, subsequently validated via experimental trials, provided the optimal working conditions to achieve a remarkable reduction of the marks from the deep-drawn feature without the occurrence of rupture.

Keywords: aluminium; hydroforming; reshaping; response surface methodology; multi-objective optimization

Citation: Piccininni, A.; Cusanno, A.; Palumbo, G.; Ingarao, G.; Fratini, L. Improving the Quality of Reshaped EoL Components by Means of Accurate Metamodels and Evolutionary Algorithms. *J. Manuf. Mater. Process.* **2024**, *8*, 253. https://doi.org/10.3390/jmmp8060253

Academic Editor: Steven Y. Liang

Received: 14 October 2024
Revised: 4 November 2024
Accepted: 5 November 2024
Published: 12 November 2024

1. Introduction

Production of just five key materials (aluminum, steel, cement, paper, aluminum, and plastic) accounts for over half of all the greenhouse gas (GHG) emissions released by industry worldwide each year [1]. The primary aluminum production process is the most energy- and emissions-intensive among the aforementioned materials [2]. The aluminum production industry is responsible for about 3% of the world's 9.4 Gt of direct industrial CO_2 emissions in 2021 [3]. Since 1971, the global demand for aluminum has increased by nearly six times; although during the COVID-19 pandemic, aluminum production fell flat, it has since started growing quickly once again, and global demand is likely to continue growing in response to the increasing global population and GDP 2021 [3]. The main approach for reducing the primary production and decoupling the resource depletion from the economic growth is the implementation of circular economy strategies [4].

The basic idea is to turn material scraps and End-of-Life (EoL) products/components directly into reusable materials or, better yet, into new products/components. Although recycling is the most commonly applied strategy when metals are concerned, it allows only the material out of EoL components to be recovered.

Moreover, it is worth remarking that for aluminum alloys, the conventional recycling route, based on remelting, is neither energy- nor resource-efficient. The main drawback of conventional recycling processes is actually the permanent material losses occurring during remelting because of oxidation [5]. In order to overcome such issues, researchers have turned to Solid State Recycling (SSR) strategies. These approaches directly turn aluminum scraps into semi-finished products by avoiding the remelting step [6]. The solid-state nature of such a process category results in no material losses due to oxidation.

To further reduce the environmental impact of industry, it is necessary to move away from recycling toward more virtuous circular economy strategies that are able to recover both materials and functions from EoL components. Specifically for metals, Cooper and Allwood proposed a framework for metal reuse in which four main strategies—relocation, cascade, remanufacturing, and reform/reshaping—are identified [7]. Remanufacturing and reshaping envisage manufacturing processes to be applied to reuse EoL components. In this respect, manufacturing scientists have to find new processes or rethink conventional processes for processing/reprocessing EoL components. In this respect, sheet metal-based components might represent a significant share of the EoL sector. It is worth remarking that sheet metal-based components account for quite a large share of the global semi-finished production. In the case of aluminum alloys, sheets (including strips and foil production) account for about 45% of the yearly global demand [8]. Therefore, finding reuse options for sheet metal-based EoL components would enable significant environmental impact reduction.

Overall, the reshaping/Reforming approach has been overlooked by the scientific community so far. Forming processes applied specifically as reuse strategies for sheet metal-based components are covered in very few scientific papers so far. Brosius et al. [9] described in a review paper how a demounted automotive engine hood can be reshaped into a rectangular sheet metal component by a sheet hydroforming process. Takano et al. [10] applied Single Point Incremental Forming (SPIF) on a flattened sheet. The reshaping they propose includes the flattening of a previously bent sheet and a subsequent incremental forming step. Some of the authors of the present paper have recently proposed a novel approach to reshaping sheet metal-based EoL components [11,12]. Specifically, SPIF was directly applied to a deep-drawn square box to change its shape. However, the SPIF approach presented by the authors allows the addition of a feature on EoL components rather than providing a brand-new shape. To tackle this challenge, the authors have recently proposed a new reshaping idea based on the Sheet Hydroforming (SHF) process. In this study, the authors replicated a reshaping route: a deep drawing process was adopted to impart a square feature; subsequently, SHF was performed to remove the feature and obtain a brand-new shape. Results proved that hydroforming can be successfully applied for reshaping proposes [13].

Nevertheless, the developed analyses revealed that reshaping process design is more challenging than conventional forming one as new design objectives and constraints need to be considered, making the process engineering more complex. Overall, it is well known that the sheet metal stamping/forming processes are characterized by conflicting design objectives [14]. The processes are driven by restraining forces; by increasing them, for instance, stringback distortions tend to decrease while maximum thinning and ductile fracture danger increase. Sheet metal forming processes have been optimized by using several multi-objective optimization techniques. Xie et al. [15] integrated the RBM–BPNN network and multi-objective particle swarm optimization (MOPSO) to design the blank holder force for a double-C part process optimization. Xiao et al. [16] proposed a new multi-objective optimization approach applied to hot stamping with partition temperature control. First, a finite element model (FEM) was established to simulate the hot stamping of an aluminum box-shaped part. Then, a multi-objective optimization approach was proposed based on a non-dominated sorting genetic algorithm (NSGA-II). Sun et al. [17] applied a multi-objective reliability-based design optimization to optimize the double-hat thin-walled structure by coupling with stamping uncertainties. Different surrogate

modeling techniques were adopted to approximate the forming and crashing responses in terms of mean and standard deviation. After that, a multi-objective particle swarm optimization (MOPSO) algorithm was employed to seek optimal, reliable design solutions, which were combined with Monte Carlo Simulation (MCS).

Hamdaoui et al. [18] coupled Kriging surrogates with NSGA-II to perform multi-objective optimization of CPU-intensive sheet metal forming applications. The approach they proposed is validated on the ZDT test functions and on a real-life industrial use case relevant to the sheet metal forming community. Oujebbour et al. [19] proposed a multi-objective optimization based on a Simulated Annealing algorithm hybridized with the Simultaneous Perturbation Stochastic Approximation. They applied this procedure to simultaneously optimize the spring back and the danger of failure in a complex sheet metal stamping process. The authors compared the performance they obtained with those provided by the well-known Nondominated Sorting Genetic Algorithm II. Some of the authors of the present paper have applied a multi-objective optimization based on an RBF response surface to design and optimize the warm hydroforming process of the AC170PX aluminum alloy [20].

The present paper proposes a multi-objective design methodology addressed to the new design challenges characterizing reshaping by hydroforming processes. As a matter of fact, together with the conventional process parameters and design objectives characterizing the conventional sheet-forming processes, reshaping process design offers new challenges. At first, the input material is, in fact, an EoL component, and it is characterized by lower formability (part of the available formability is already used in the primary process) and a higher rigidity compared with the flat undeformed sheet in conventional stamping. This makes the reshaping process more complex to be designed. Secondly, the reshaping process has one more design objective: to completely remove the original shape (the one provided by the primary process). The above-mentioned aspects raise new challenges in the sheet metal forming process design. In this paper, for the first time, a multi-objective approach is applied to reshaping processes. Taking advantage of a benchmark study that was already investigated by the authors, an ordered plan of simulations was run, and the results were used to train accurate metamodel on output quantity descriptive of the problem: the height of the residual mark from the deep drawing step (ΔH) and the maximum strain severity (expressed by the output variable $FLDCRT_{max}$). The trained metamodels, used as the base for a subsequent virtual optimization managed by multi-objective Evolutionary Algorithms (EA), allowed to determine the optimal reshaping conditions to improve the overall quality of the reshaped part (minimization of the residual marks from the previous forming step) and, at the same time, preserve the integrity of the final component (no occurrence of rupture). Experimental trials were eventually carried out to validate the prediction from the optimization round.

2. Materials and Methods

2.1. The Reshaping Approach

The basic principle of the reshaping approach is here briefly recalled: an EoL component, whose current geometry is the result of a specific manufacturing process, is subjected to an additional step of deformation and brought to a new geometry. In the present work, a 0.5 mm AA5754-H22 blank was initially subjected to a deep drawing step, and the formed part was considered the EoL component. Subsequently, the hydroforming process was applied to change the geometry of the component to a more complex shape. The scheme in Figure 1 describes the sequence of the steps related to the reshaping approach. In previous work from the same authors [13], it was also investigated how the positioning of the deep-drawn feature could have an influence on the final quality of the reshaped components: in fact, aside from changing the geometry of the EoL component without the occurrence of rupture, it was also important to eliminate any residual mark from the previous geometry. As a consequence, a list of guidelines was also drawn: in particular, it was concluded that the restraining force has to be modulated according to the level of deformation that is

expected to be imparted during the reshaping process. In fact, inducing enough stretching in a region where the secondary plastic deformation is expected not to be excessive could be a solution to completely remove the existing feature from the previous manufacturing step.

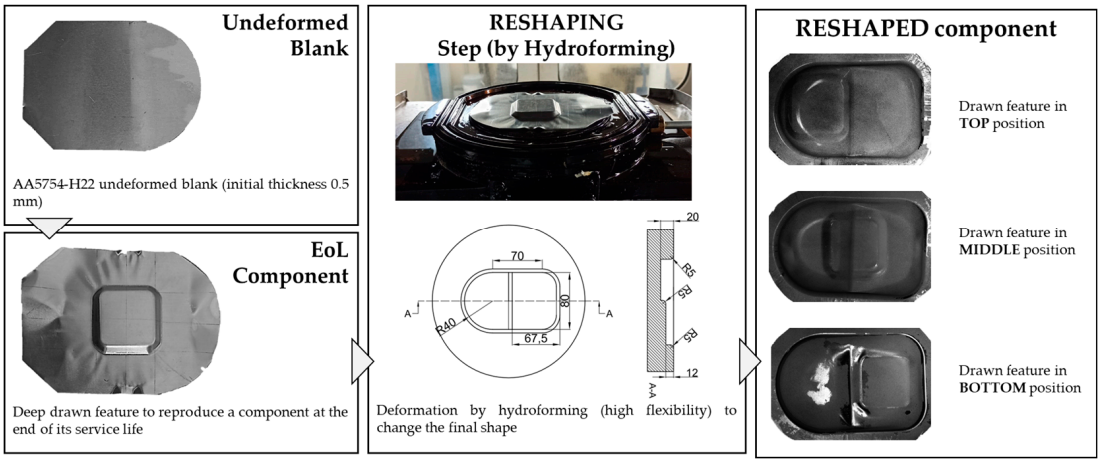

Figure 1. General overview of the reshaping approach.

The authors, in fact, demonstrated that when the deep-drawn feature was positioned at the BOTTOM location, the mark of the existing feature was still evident after the reshaping by hydroforming. Therefore, the aim of the present work is to identify the optimal values of the reshaping process parameters to improve the final quality of the reshaped component (minimization of the residual marks without the occurrence of rupture during the reshaping step).

2.2. Optimization of the Reshaping Process

Using the same numerical approach detailed in [13], the attention was focused on one of the investigated conditions (labeled as ID06), namely the one characterized by the drawn feature located in the BOTTOM position and reshaped by hydroforming under a blank holder force (BHF) increasing from 13 kN to 77 kN and setting the oil pressure from 1 bar to 52 bar. Starting from this condition, a full factorial DoE was created and composed of 16 designs by changing the average BHF value (BHF_{avg}) and the maximum oil pressure over four levels. The investigated conditions are listed in Table 1.

Table 1. Full Factorial DoE plan of numerical simulations.

ID	BHF_{in} [kN]	BHF_{fin} [kN]	BHF_{avg} [kN]	p_{max} [bar]
1	23	87	55	52
2	23	87	55	104
3	23	87	55	156
4	23	87	55	208
5	33	97	65	52
6	33	97	65	104
7	33	97	65	156
8	33	97	65	208
9	43	107	75	52
10	43	107	75	104
11	43	107	75	156
12	43	107	75	208
13	53	117	85	52
14	53	117	85	104
15	53	117	85	156
16	53	117	85	208

As can be seen, the initial and final values of the BHF were increased by the same quantity, thus keeping the same slope of the ID06. Numerical results were analyzed in terms of two variables: (i) ΔH, defined as the residual height of the deep-drawn feature after the reshaping by hydroforming (see Figure 2a), and (ii) the maximum value of the field variable FLDCRT [21]. More in detail, the latter variables describe the current severity of the deformation state in a single node by calculating the ratio of the current nodal major strain and the limit major strain on the material forming limit curve for the same value of the minor principal strain: when the FLDCRT value is equal to 1 (or higher), the model predicts the initiation of the damage.

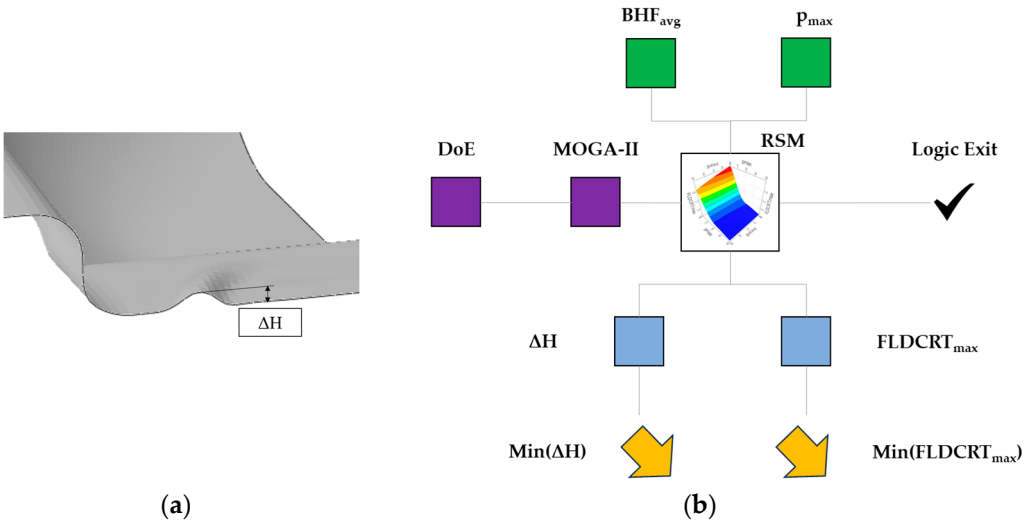

Figure 2. Optimization process: (**a**) definition of the DH output variable and (**b**) overview of the workflow.

The optimization procedure, whose workflow is schematically depicted in Figure 2b, was created in the working environment of a dedicated integration platform (modeFRONTIER) and was based on two main steps. At first, an accurate metamodel linking the defined input variables to the outputs was created: this first step was accomplished by training accurate Response Surfaces (RS). Two algorithms were chosen in the RS training: (i) the anisotropic Kriging model, originally developed in geostatistics [22,23], and (ii) the Radial Basis Functions [24].

Once the training was completed, the RS was used as the base for the subsequent optimization, which was managed by an evolutionary algorithm (EA) [25,26] that is particularly suitable for the solution of multi-objective problems. The general principle of an evolutionary algorithm is the reproduction of the "survival of the fittest" principle; therefore, EAs perform optimization or learning tasks with the ability to evolve. Moreover, three main aspects are distinctive: EAs are (i) population-based, since they maintain a group of solutions, called a population, to optimize the problem; (ii) fitness-oriented, since EAs prefer fitter individuals to converge the optimization, i.e., individuals whose fitness value is higher; (iii) variation-driven since the individual's genes are recombined mimicking the genetic gene changes to converge to the final solution [27].

In the present work, the attention was focused on two EAs, namely the MOGA-II and the NSGA-II. The optimization based on the trained RS is generally classified as "virtual": in fact, all the individuals that were created by the EAs were virtually extrapolated (i.e., no additional simulations were run). As can be seen in Figure 2b, the workflow was completed by the two objective functions, one for each output variable; therefore, the main goal of the optimization was to reduce as possible the evidence of the deep-drawn feature (i.e., the minimization of the ΔH) avoiding, at the same time, the occurrence of rupture (i.e., the minimization of the maximum value of the FLDCRT parameter).

2.3. Final Validation

The prediction from the optimization step was validated at two levels: at first, the optimal virtual design was simulated, and the numerical value of the output parameters was compared with the prediction from the optimization step. Furthermore, the combination of process parameters that were identified as optimal—i.e., able to ensure a compromise between the minimization of the residual marks from the DD step (minimization of ΔH) and avoiding the occurrence of rupture ($FLDCRT_{max}$ lower than 1)—was eventually reproduced via experimental trials.

First, the deep drawing (DD) process was performed at room temperature on undeformed AA5754 blanks with an optimized shape (Figure 3a) under a linearly increasing BHF from 2 kN to 4.2 kN and a constant punch velocity of 1 mm/s and using a Galdabini Quasar 600 hydraulic press; the 3D reproduction of the final blank shape after the DD step is shown in Figure 3b. After that, the blank was reshaped using a 2500 kN prototype electro-hydraulic press machine (details of the adopted equipment are reported in [13]) into a new geometry (shown in Figure 3c). The obtained reshaped component was cut along a plane in the thickness direction, crossing the fillet radius of the DD feature (Figure 3d).

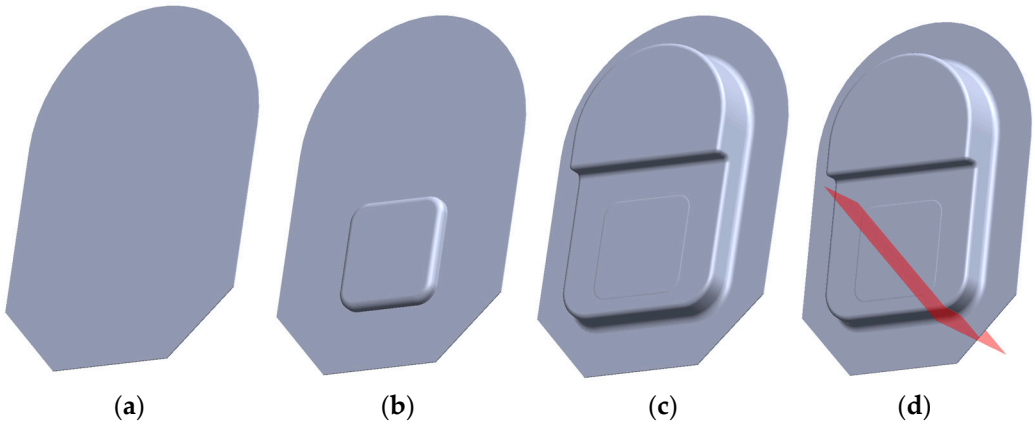

Figure 3. AA5754 (**a**) undeformed blank; (**b**) shape after the deep drawing (DD) step; (**c**) shape the reshaping process (**d**) Cutting plane (highlighted in red), used to measure the residual ΔH.

Then, the residual height of the deep-drawn feature after the reshaping step (ΔH), as well as the thickness distribution in the corner area, were measured.

3. Results and Discussion

3.1. Training of the Response Surfaces: The Anisotropic Kriging Formulation

As anticipated in Section 2.2, the values of the two output variables were fitted using two algorithms. Regardless of the adopted formulation, the whole data set was subdivided into two groups: (i) the training set (approximately equal to 80% of the designs) and (ii) the validation set (composed of the remaining 20%). The former was used to actually train the RS, whereas the latter was used to evaluate the predictive capabilities of the metamodel.

When the anisotropic Kriging formulation was considered, the variogram type and its policy could be set. In particular, the variogram model—which represents the distributional model that fits the data and visually depicts the covariance between each pair of points belonging to the sample data—could be set as Gaussian or exponential. As for the variogram policy, the variogram parameters could be automatically set to (i) maximize its likelihood, which means to maximize the probability that a statistical distribution associated with the variogram parameters could generate the given dataset, or (ii) maximize the leave-one-out (LOO) predictive probability, where such a probability gives a measure of the goodness of the model by removing one point at a time from the dataset and estimating the value at the removed site on the basis of the remaining designs. In light of this, different combinations of variogram type and policy were investigated on both the output variables, and the performance of each combination was compared. Results are resumed in Table 2 for the

output variable ΔH; the performance index "Mean absolute error" was calculated as the average value of the difference between real and virtual designs, whereas the "R-squared" index is a coefficient of determination serving as a statistical measure of how well the regression model approximates real data.

Table 2. ΔH output variable: RSM validation table (anisotropic Kriging formulation).

ID	Variogram Type	Variogram Policy	Mean Absolute Error	R-Squared
AKR_ΔH_1	Gaussian	Maximizing likelihood	5.16×10^{-2} mm	0.972
AKR_ΔH_2	Gaussian	Maximizing LOO probability	1.40×10^{-1} mm	0.854
AKR_ΔH_3	Exponential	Maximizing likelihood	1.40×10^{-1} mm	0.811
AKR_ΔH_4	Exponential	Maximizing LOO probability	1.52×10^{-1} mm	0.778

The Gaussian variogram combined with the policy of maximizing its likelihood led to the lowest absolute error and highest R-squared. Similar results were found on the other output variable ($FLDCRT_{max}$); the comparison of the indices for each combination is detailed in Table 3.

Table 3. $FLDCRT_{max}$ output variable: RSM validation table (anisotropic Kriging formulation).

ID	Variogram Type	Variogram Policy	Mean Absolute Error	R-Squared
AKR_FLDCRT_1	Gaussian	Maximizing likelihood	5.18×10^{-3} mm	0.999
AKR_FLDCRT_2	Gaussian	Maximizing LOO probability	2.44×10^{-2} mm	0.982
AKR_FLDCRT_3	Exponential	Maximizing likelihood	8.88×10^{-2} mm	0.722
AKR_FLDCRT_4	Exponential	Maximizing LOO probability	9.03×10^{-2} mm	0.719

The visual representation of the calibrated metamodels for both the output variables is reported in Figure 4. The two RS suggest that, for low values of the maximum oil pressure, the maximum FLDCRT value is far below 1, but the existing feature cannot be completely removed (the ΔH is around 1.8 mm). On the other hand, if increasing the restraining forces, the residual mark from the drawn feature tends to reduce, but at the same time, the severity of the strain conditions worsens, and the rupture is more likely to occur (values well over 1).

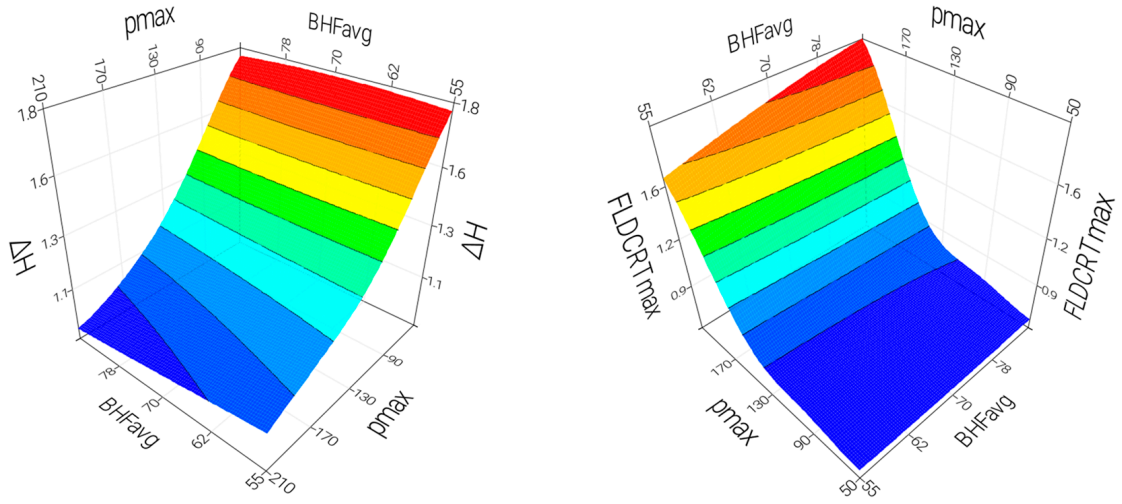

Figure 4. Visual representation of the trained metamodels (anisotropic Kriging algorithm): (**a**) ΔH and (**b**) $FLDCRT_{max}$ output variables. Colored zones, from blue to red, refer to increasing value of the two output variables.

3.2. Training of the Response Surfaces: The Radial Basis Function Kernel

Aside from the anisotropic Kriging formulation, the collected data were also fitted by using the Radial Basis Functions. The adopted integration platform allows one to select among five different kernels. The choice of the best-performing algorithm was made at first by checking that the Mean Leave-One-Out Error (MLOOE) was lower than 0.2 (considered the threshold value over which the kernel ends with a bad fitting of the data set). The MLOOE was calculated by excluding, in turn, one point belonging to the training set and comparing its value with the predicted one; therefore, the smaller the MLOOE, the more accurate the training. After this first check, the performance of the five kernels was compared in terms of the same indices presented in Section 3.1. Results for the output variable ΔH are reported in Table 4 (ordered in descending level of performance).

Table 4. ΔH output variable: RSM validation table (Radial Basis Function formulation).

ID	Kernel	Mean Absolute Error	R-Squared
RBF_ΔH_CS	Wendland's Compactly Supported	5.66×10^{-2} mm	0.970
RBF_ΔH_PS	Duchon's Polyharmonic Splines	6.37×10^{-2} mm	0.954
RBF_ΔH_MQ	Hardy's MultiQuadrics	7.56×10^{-2} mm	0.952
RBF_ΔH_IMQ	Inverse MultiQuadrics	9.38×10^{-2} mm	0.930
RBF_ΔH_G	Gaussians	1.49×10^{-1} mm	0.836

The Wendland's Compactly Supported algorithm was identified as the best one due to the lowest mean absolute error and the highest correlation coefficient. The same approach was used on the other output variable, for which Duchon's Polyharmonic Splines was selected as the best-fitting kernel (see the value reported in Table 5).

Table 5. $FLDCRT_{max}$ output variable: RSM validation table (Radial Basis Function formulation).

ID	Kernel	Mean Absolute Error	R-Squared
RBF_FLDCRT_PS	Duchon's Polyharmonic Splines	3.09×10^{-2} mm	0.964
RBF_ΔH_MQ	Hardy's MultiQuadrics	4.58×10^{-2} mm	0.941
RBF_ΔH_CS	Wendland's Compactly Supported	7.02×10^{-2} mm	0.874
RBF_ΔH_IMQ	Inverse MultiQuadrics	7.12×10^{-2} mm	0.854
RBF_ΔH_G	Gaussians	1.03×10^{-1} mm	0.693

The 3D visualization of the trained metamodels provided similar considerations to those reported in Section 3.1. The two RS shown in Figure 5a,b confirmed that keeping the restraining force (BHF) low is beneficial to limit the severity of the strain condition but not for the elimination of the deep-drawn feature. On the contrary, combining the high value of the BHF with the high oil pressure allows us to satisfy only one of the two objective functions (minimization of the output variable ΔH).

3.3. Results from the Optimization Rounds

As detailed in Section 2.2, two EAs were considered for the optimization based on the trained RS. In both cases, a number of 1000 successive generations was defined. Thus, the optimization round evolved throughout 16,000 individuals: even though it may seem a large number, the computational cost was extremely limited since the designs were all virtually created. The results of the optimization were analyzed by plotting the distribution of the individuals in a bubble chart: the two output variables are reported on the axes, whereas the color of the bubble refers to the input variable. As an example, results from the optimization managed by the MOGA-II algorithms using the RS trained with the anisotropic Kriging formulation are shown in Figure 6.

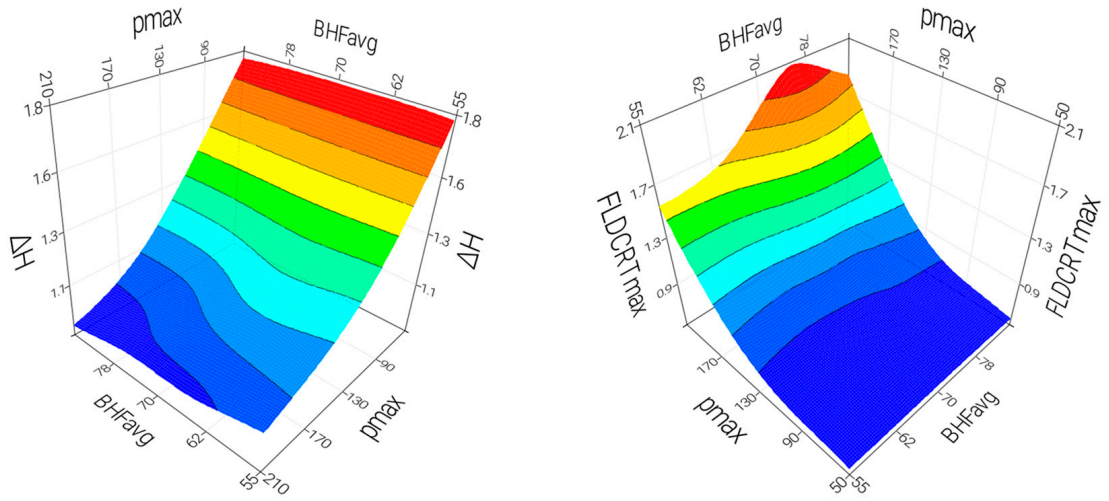

(**a**) (**b**)

Figure 5. Visual representation of the trained metamodels (Radial Basis Function algorithm): (**a**) ΔH and (**b**) $FLDCRT_{max}$ output variables. Colored zones, from blue to red, refer to increasing value of the two output variables.

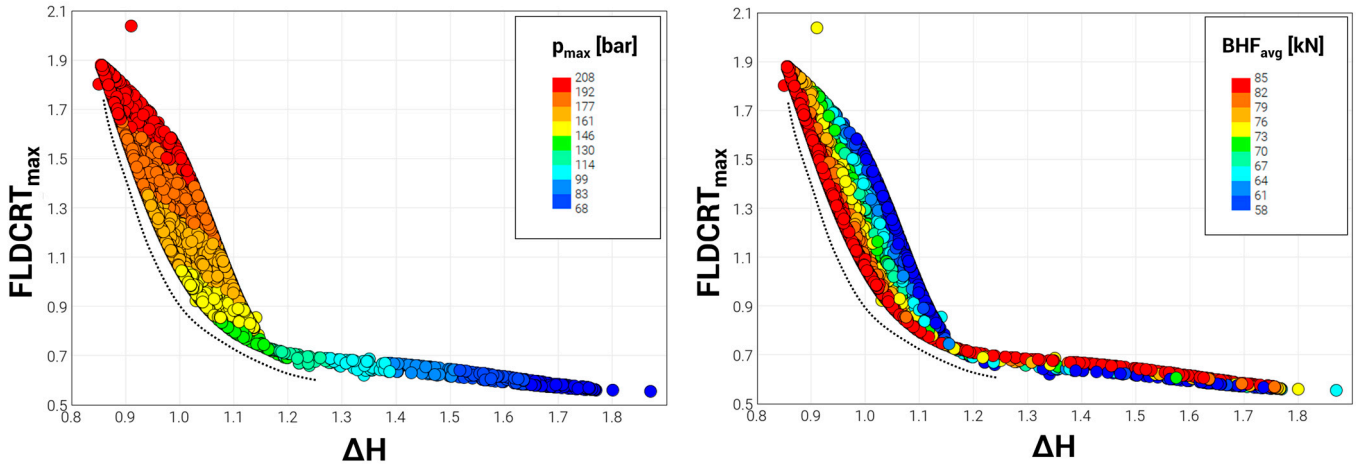

(**a**) (**b**)

Figure 6. Optimization results (RS trained using the AKR model and MOGA-II as EA): distribution of the created designs in terms of (**a**) maximum oil pressure and (**b**) average value of the BHF.

The designs belonging to the Pareto front (those close to the black dashed line) are defined as non-dominated designs, which means that it is not possible to find another solution within the front that is able to improve the two objectives simultaneously. If focusing attention on the plot of Figure 6a, Pareto designs are characterized by values of the p_{max} ranging from 130 bar up to 208 bar and a high value of the BHF (red-colored bubbles in Figure 6b). Therefore, the optimization suggested that the restraining force had to be set at the maximum value, whereas the pressure could be varied over different levels. It should be underlined that, despite the Pareto designs representing optimal solutions, they are not always physically acceptable, as in the case of those characterized by values of the $FLDCRT_{max}$ higher than the threshold value of 1. Therefore, it became necessary to isolate a sub-group of the Pareto front containing all the designs that could simultaneously lead to a remarkable reduction of the residuals from the deep-drawn feature (minimization of ΔH) and avoid the occurrence of rupture during the reshaping by hydroforming ($FLDCRT_{max}$ lower or as close as possible to 1). To do this, Pareto front designs were plotted in the

parallel coordinate chart, where input and output variables are indicated by equally spaced parallel vertical axes and each design by a polyline. As shown in Figure 7, by filtering the values on the $FLDCRT_{max}$ axis, it was possible to conclude that setting the average restraining force around 80 kN and the maximum oil pressure higher than 150 bar, a sound-reshaped component with limited residual marks from the deep-drawn feature could be obtained.

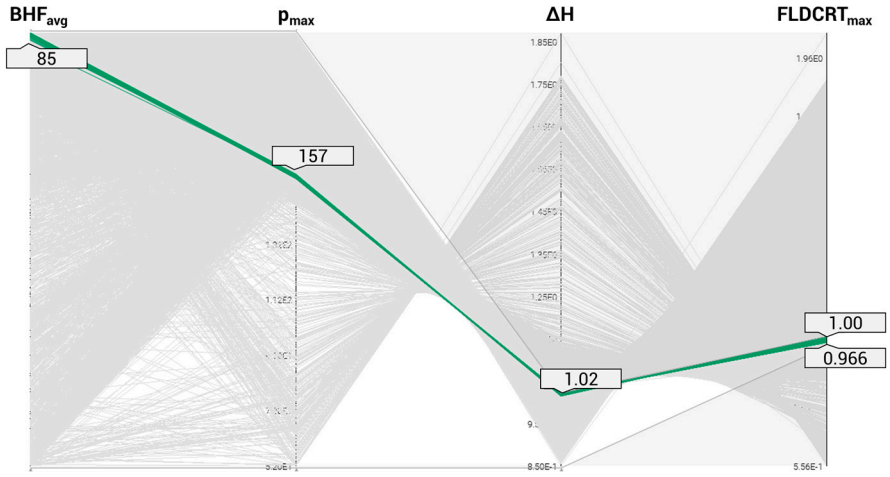

Figure 7. Optimization results (RS trained using the AKR model and MOGA-II as EA): parallel coordinate chart.

The same analysis was carried out also for the other three RS/EA combinations: the optimal design from each optimization was identified as the one characterized by the lowest value of the $FLDCRT_{max}$ parameter. Table 6 suggests that, regardless of the RS/EA combination, the optimal values of the hydroforming parameters imply a strain condition quite close to the limit, ending in a comparable reduction of the deep-drawn feature (the difference among the predicted ΔH values was in the order of thousandths of mm).

Table 6. Comparison among the optimal designs from the different RS/EA combinations.

Opt. ID	RS Algorithm	EA	$(p_{max})_{opt}$	$(BHF_{avg})_{opt}$	ΔH	$FLDCRT_{max}$
AKR_MOGA-II	Anisotropic Kriging	MOGA-II	157 bar	85 kN	1.015 mm	1.000
AKR_NSGA-II	Anisotropic Kriging	NSGA-II	157 bar	85 kN	1.016 mm	0.999
RBF_MOGA-II	Radial Basis Function	MOGA-II	159 bar	77 kN	1.006 mm	0.999
RBF_NSGA-II	Radial Basis Function	NSGA-II	153 bar	82 kN	1.020 mm	0.998

At the same time, it should also be noted that when data were fitted by the anisotropic Kriging formulation, the optimization results were almost identical, irrespective of the adopted EA. On the other hand, small differences were recorded when using the RS trained with the RBF algorithm. Such a difference may be related to the lower values of the R-squared index of the RS trained with the RBF compared to the anisotropic Kriging.

Moreover, analogous differences were also found when comparing the shape of the Pareto fronts from the four combinations (see Figure 8).

Within the design space of the physically acceptable Pareto designs ($FLDCRT_{max}$ lower than 1), fitting the data with the anisotropic Kriging led to almost overlapped fronts, whereas the other two fronts (circular marker) were located in different areas. Among the four optimal designs listed in Table 6, the one identified by the ID "RBF_MOGA-II" was eventually validated since being characterized by the lowest value of the height of the residual mark (ΔH) and severity of the strain condition below the threshold value (FLDCRT lower than 1).

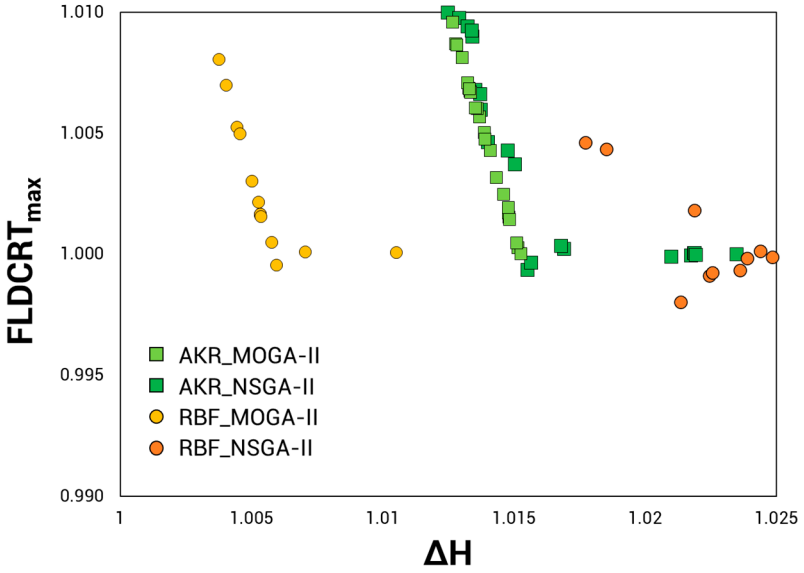

Figure 8. Comparison of the four Pareto fronts.

3.4. Validation of the Optimization Results

As described in Section 2.3, the identified optimal design (RBF_MOGA-II) was validated at two different levels. At first, an additional FE simulation implementing the predicted optimal values of the BHF and oil pressure was run. On the deformed blank, two nodes (labeled as A and B in Figure 9a) were chosen to evaluate the residual mark from the DD step: the distance along the vertical direction was equal to 0.81 mm, around 19% lower than the predicted one (1.006 mm). Despite a non-negligible discrepancy, the results could be considered valid and conservative since the regression model overestimated the ΔH value. Such overestimation was likely to be related to an overestimation of the regression model in a region of the design space close to the optimal design. As for the other output, the simulated best design showed a maximum value of the FLDCRT (0.99) that was extremely close to the predicted one (0.999).

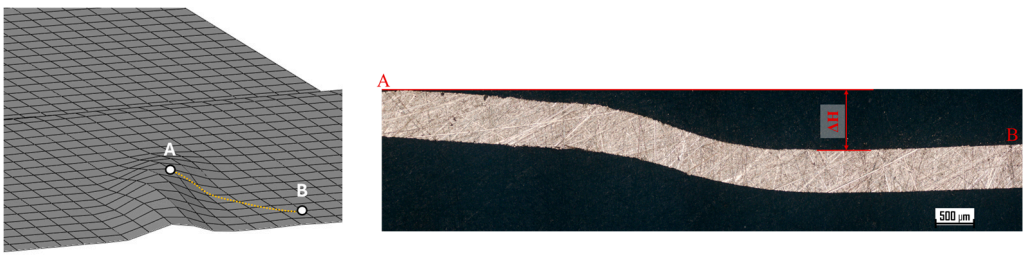

(**a**) (**b**)

Figure 9. Optimization results: (**a**) numerical estimation of the ΔH from the optimal design; (**b**) cross-section of the extracted sample from the reshaped blank (the investigated path starts from point A and ends at point B).

The best design was eventually validated via experimental hydroforming tests: the BHF was increased from 45 kN to 109 kN (BHF_{avg} = 77 kN) while raising the pressure up to 159 bar with a rate of 1 bar/s. At the end of the test, a portion of the formed blank containing the residual mark was isolated and inspected at the optical microscope (see Figure 9b): it is evident that the left part of the investigated portion kept a higher thickness due to the hardening from the deep drawing step. At first, the height of the residual mark from the DD step was calculated, and the result was 0.79 mm, quite close to the predicted value from the simulation of validation. To further validate the accuracy of the predicted

values, the thickness was measured along the extracted blank portion and compared with the numerical values from the path indicated by the yellow dashed line in Figure 9a. The comparison shown in Figure 10 demonstrates a good correspondence between numerical and experimental data with an average discrepancy of around 6% (with a maximum error of 14%).

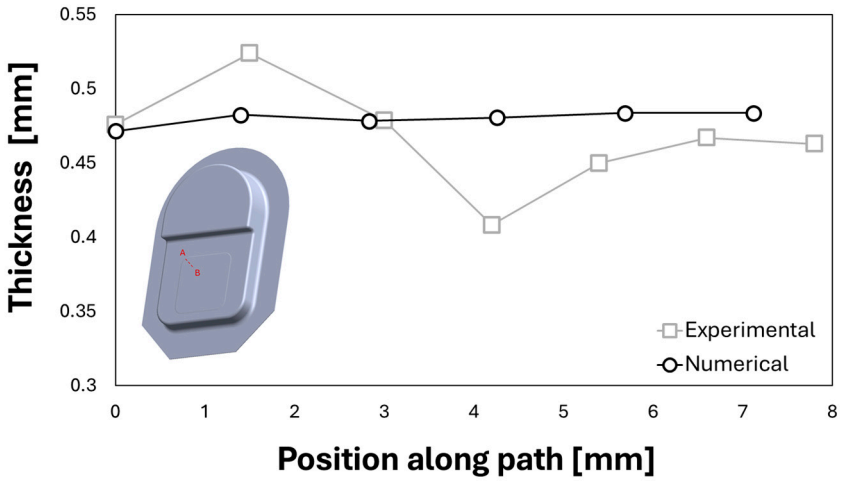

Figure 10. Validation of the optimization: comparison of the thickness distribution along the investigated blank portion (A is the start node, B the end node).

4. Conclusions

In the present paper, the potentialities of the reshaping approach have been further deepened by proposing a methodology to optimize the overall quality of a reshaped part. According to the current state-of-the-art reshaping approach, general guidelines exist, but none of them suggest how much further the effectiveness of the reshaping can be pushed and, therefore, what the percentage of success in completely removing a pre-existing feature from an EoL part is.

In the present work, by taking advantage of a case study already investigated by the authors, the overall quality of the reshaped part was optimized: a blank with a deep-drawn feature (simulating the EoL) was deformed by hydroforming. The deep-drawn feature was intentionally located in a non-favorable region where lower strains were expected to be imparted during the reshaping step. In light of this, the optimization aimed at determining the best working conditions to eliminate any residuals from the previous deep drawing step and, at the same time, preserving the integrity of the final reshaped part.

The metamodels trained on the data from a full factorial DoE plan of simulations allowed the expression of the output variables (ΔH and $FLDCRT_{max}$) as a function of the average BHF and the maximum oil pressure. The subsequent virtual optimization suggested that increasing too much the restraining action exerted by the blank holder led to a more evident elimination of the residual mark but, at the same time, to worse deformation conditions in other regions of the blank. Regardless of the specific combination between the metamodel algorithms and the EA, a successful and optimized reshaping was predicted if an average value of the BHF was set at close to 80 kN and the maximum pressure was higher than 150 bar. Those optimal conditions, predicted by the EA, were at first numerically validated: it was found that the virtual design overestimated the ΔH of about 19% (predicted value of 1.006 mm, the simulated value equal to 0.81 mm).

Eventually, the experimental validation was carried out: a sound-shaped blank was obtained, characterized by a residual height of the deep-drawn feature equal to 0.79 mm (quite close to the one predicted by the numerical simulation). In addition, the absence of rupture indirectly validated also the predicted value of the $FLDCRT_{max}$. To further confirm the accuracy of the numerical prediction, the thickness distribution along a diagonal direc-

tion passing through the residual mark was compared with the numerical data showing a high level of correspondence (average error around 6%).

The proposed methodology provides an additional brick of knowledge for the reshaping by hydroforming, demonstrating that the process conditions can be tailored to optimize the overall quality of the reshaped parts, taking into account the geometry of the pre-existing feature to be eliminated and the level of strain imparted during the reshaping step. The methodology is flexible enough to be applied to a wide range of scenarios involving different materials, die geometries, and process conditions.

Author Contributions: Conceptualization, A.P., G.I., G.P. and L.F.; methodology, A.P., A.C, G.I., G.P. and L.F.; software, A.P. and A.C.; validation, A.P., A.C., G.I., G.P. and L.F.; formal analysis, A.P., A.C. and G.I.; investigation, A.P., A.C. and G.I.; data curation, A.P., A.C. and G.I.; writing—original draft preparation, A.P., A.C. and G.I.; writing—review and editing, G.P. and L.F.; visualization, A.P. and A.C.; supervision, G.P. and L.F.; project administration, G.P. and L.F. All authors have read and agreed to the published version of the manuscript.

Funding: This research received no external funding.

Data Availability Statement: Data and optimization code will be made available upon request to interested researchers.

Acknowledgments: The activities have been financed by the European Union—NextGenerationEU (National Sustainable Mobility Center CN00000023, Italian Ministry of University and Research Decree n. 1033—17/06/2022, Spoke 11—Innovative Materials and Lightweighting). The opinions expressed are those of the authors only and should not be considered representative of the European Union or the European Commission's official position. Neither the European Union nor the European Commission can be held responsible for them.

Conflicts of Interest: The authors declare no conflict of interest.

References

1. Oberhausen, G.; Zhu, Y.; Cooper, D.R. Reducing the environmental impacts of aluminum extrusion. *Resour. Conserv. Recycl.* **2022**, *179*, 106120. [CrossRef]
2. Ashby, M.F. (Ed.) Materials and Environment. In *Butterworth-Heinemann*, 3rd ed.; Elsevier: Amsterdam, The Netherlands, 2021; pp. 41–64, ISBN 978-0-12-821521-0.
3. IEA. Available online: https://www.iea.org/reports/aluminium (accessed on 15 March 2024).
4. Tolio, T.; Bernard, A.; Colledani, M.; Kara, S.; Seliger, G.; Duflou, J.; Battaia, O.; Takata, S. Design, management and control of demanufacturing and remanufacturing systems. *CIRP Ann.* **2017**, *66*, 585–609. [CrossRef]
5. Duflou, J.R.; Tekkaya, A.E.; Haase, M.; Welo, T.; Vanmeensel, K.; Kellens, K.; Dewulf, W.; Paraskevas, D. Environmental assessment of solid state recycling routes for aluminium alloys: Can solid state processes significantly reduce the environmental impact of aluminium recycling? *CIRP Ann.* **2015**, *64*, 37–40. [CrossRef]
6. Wan, B.; Chen, W.; Lu, T.; Liu, F.; Jiang, Z.; Mao, M. Review of solid state recycling of aluminum chips. *Resour. Conserv. Recycl.* **2017**, *125*, 37–47. [CrossRef]
7. Cooper, D.R.; Allwood, J.M. Reusing Steel and Aluminum Components at End of Product Life. *Environ. Sci. Technol.* **2012**, *46*, 10334–10340. [CrossRef] [PubMed]
8. Cullen, J.M.; Allwood, J.M. Mapping the Global Flow of Aluminum: From Liquid Aluminum to End-Use Goods. *Environ. Sci. Technol.* **2013**, *47*, 3057–3064. [CrossRef]
9. Brosius, A.; Hermes, M.; Ben Khalifa, N.; Trompeter, M.; Tekkaya, A.E. Innovation by forming technology: Motivation for research. *Int. J. Mater. Form.* **2009**, *2*, 29–38. [CrossRef]
10. Takano, H.; Kitazawa, K.; Goto, T. Incremental forming of nonuniform sheet metal: Possibility of cold recycling process of sheet metal waste. *Int. J. Mach. Tools Manuf.* **2008**, *48*, 477–482. [CrossRef]
11. Ingarao, G.; Zaheer, O.; Campanella, D.; Fratini, L. Re-forming end-of-life components through single point incremental forming. *Manuf. Lett.* **2020**, *24*, 132–135. [CrossRef]
12. Ingarao, G.; Zaheer, O.; Fratini, L. Manufacturing processes as material and energy efficiency strategies enablers: The case of Single Point Incremental Forming to reshape end-of-life metal components. *CIRP J. Manuf. Sci. Technol.* **2021**, *32*, 145–153. [CrossRef]
13. Piccininni, A.; Cusanno, A.; Palumbo, G.; Zaheer, O.; Ingarao, G.; Fratini, L. Reshaping End-of-Life components by sheet hydroforming: An experimental and numerical analysis. *J. Mater. Process. Technol.* **2022**, *306*, 117650. [CrossRef]
14. Ingarao, G.; Di Lorenzo, R. A new progressive design methodology for complex sheet metal stamping operations: Coupling spatially differentiated restraining forces approach and multi-objective optimization. *Comput. Struct.* **2010**, *88*, 625–638. [CrossRef]

15. Xie, Y.; Du, L.; Zhao, J.; Liu, C.; Li, W. Multi-objective optimization of process parameters in stamping based on an improved RBM–BPNN network and MOPSO algorithm. *Struct. Multidiscip. Optim.* **2021**, *64*, 4209–4235. [CrossRef]
16. Xiao, W.; Cai, H.; Lu, W.; Li, Y.; Zheng, K.; Wu, Y. Multi-objective optimization with automatic simulation for partition temperature control in aluminum hot stamping process. *Struct. Multidiscip. Optim.* **2022**, *65*, 84. [CrossRef]
17. Sun, G.; Zhang, H.; Wang, R.; Lv, X.; Li, Q. Multiobjective reliability-based optimization for crashworthy structures coupled with metal forming process. *Struct. Multidiscip. Optim.* **2017**, *56*, 1571–1587. [CrossRef]
18. Hamdaoui, M.; Oujebbour, F.-Z.; Habbal, A.; Breitkopf, P.; Villon, P. Kriging surrogates for evolutionary multi-objective optimization of CPU intensive sheet metal forming applications. *Int. J. Mater. Form.* **2015**, *8*, 469–480. [CrossRef]
19. Oujebbour, F.Z.; Habbal, A.; Ellaia, R. Optimization of stamping process parameters to predict and reduce springback and failure criterion. *Struct. Multidiscip. Optim.* **2015**, *51*, 495–514. [CrossRef]
20. Palumbo, G.; Piccininni, A.; Guglielmi, P.; Di Michele, G. Warm HydroForming of the heat treatable aluminium alloy AC170PX. *J. Manuf. Process.* **2015**, *20*, 24–32. [CrossRef]
21. Dassault Systems Abaqus Analysis User's Manual. 2017.
22. Oliver, M.A.; Webster, R. A tutorial guide to geostatistics: Computing and modelling variograms and kriging. *Catena* **2014**, *113*, 56–69. [CrossRef]
23. Hansen, R.O. Interpretive gridding by anisotropic kriging. *Geophysics* **1993**, *58*, 1491–1497. [CrossRef]
24. Hussain, M.F.; Barton, R.R.; Joshi, S.B. Metamodeling: Radial basis functions, versus polynomials. *Eur. J. Oper. Res.* **2002**, *138*, 142–154. [CrossRef]
25. Bäck, T.; Schwefel, H. An Overview of Evolutionary Algorithms for Parameter Optimization. *Evol. Comput.* **1993**, *1*, 1–23. [CrossRef]
26. Fonseca, C.M.; Fleming, P.J. An Overview of Evolutionary Algorithms in Multiobjective Optimization. *Evol. Comput.* **1995**, *3*, 1–16. [CrossRef]
27. Yu, X.; Gen, M. *Introduction to Evolutionary Algorithms*; Springer-Verlag: London, UK, 2010; Volume 9, ISBN 9781849961288.